Research papers

A novel Dual Fractional-Order Extended Kalman Filter for the improved estimation of battery state of charge

Pablo Rodríguez-Iturriaga [a,*], Jorge Alonso-del-Valle [b], Salvador Rodríguez-Bolívar [a], David Anseán [b], Juan Carlos Viera [b], Juan Antonio López-Villanueva [a]

[a] Department of Electronics and Computer Technology, Faculty of Sciences, Granada, 18071, Andalusia, Spain
[b] Department of Electrical Engineering, Polytechnic School of Engineering, Gijon, 33204, Asturias, Spain

ARTICLE INFO

ABSTRACT

Fractional-order models are gaining increasing relevance in battery modeling in light of the experimental measurements from Electrochemical Impedance Spectroscopy (EIS) tests, unequivocally indicating the presence of equivalent circuit components with an impedance of non-integer order. To attain their discrete state-space representation, the approach based on the Grünwald–Letnikov (GL) definition of the fractional derivative has been widely used, albeit its applicability beyond driving cycles remains open to discussion. In this article, we present a novel Dual Fractional-Order Extended Kalman Filter (DFOEKF) for the simultaneous estimation of State of Charge (SOC) and all fractional parameters, based on the multiple-RC approximation instead. We discuss the parameter identification of fractional-order elements on a NMC811/Si-Gr cell from both frequency and time-domain data, highlighting the importance of EIS measurements for the search of appropriate time-domain values. We validate the performance of this method experimentally at different operation stages, as well as its robustness to incorrect initializations, obtaining a SOC root-mean-square (RMS) error of 0.28% and a voltage RMS error of 15.2 mV in 20 complete charge–discharge cycles. The greatly accurate estimation results both within and outside the driving cycle stage make this method an interesting alternative for the fractional modeling of LIBs in online applications.

1. Introduction

After continuous improvement over the last forty-five years [1], rechargeable lithium-ion batteries (LIBs) have become the leading technology in the electrochemical energy storage market, from portable electronics to applications in renewable energies and electric vehicles [2,3]. Their preeminence is expected to continue and even increase due to their potential decreasing costs following manufacturing upscale [4]. Therefore, the study and development of accurate battery models proves to be essential for the implementation of Battery Management Systems (BMSs) [5]. Three main categories are usually considered regarding battery models: physics-based models, data-driven models and equivalent circuit models (ECMs) [6,7]. The former attempt to reflect the physical and electrochemical processes that take place during cell operation [8–10]. Nevertheless, the computational requirements may be inappropriate for online applications, and the precise determination of physical parameters from non-destructive measurements still remains a challenging problem [11]. Conversely, data-driven models replace the battery with a black-box model that reproduces its behavior and is able to retain complex features at a moderate computational cost [12]. However, the accuracy of the model largely depends on the training dataset, which must be sufficiently extensive and representative. This may lead to an extremely time-consuming training process, which can possibly hinder their usage in practical applications [13].

On the other hand, ECMs remain the most popular choice for BMSs because of their low computational load and simple parameterization, along with the facility to implement battery estimation and noise correction algorithms [14–16]. In spite of this, many authors have pointed out their lack of meaningful physical insight, as well as their inability to model battery behavior accurately under different operating conditions [17]. For this reason, there have been numerous research efforts to develop physics-informed ECMs that account for the underlying physical processes occurring inside the cell in different manners [6,18], while maintaining a reduced computational cost in order to keep them suitable for online applications. Given that diffusion and charge transfer processes take place during battery operation, fractional calculus has recently gained popularity as an alternative tool for battery modeling, in the same way as in other physical and biological phenomena

[19–21], since fractional-order differential equations have been found to model spatially distributed relaxation processes accurately.

Regarding battery modeling, this entails the introduction of circuit elements whose electrical impedance depends on frequency according to a non-integer power law, such as constant-phase elements (CPEs). The parallel connection of a resistor and a CPE is known as a ZARC element [22], which naturally replaces the parallel-RC network that is ubiquitous in ECMs for battery monitoring systems. This is experimentally justified as well by the unequivocal non-integer behavior observed in Electrochemical Impedance Spectroscopy (EIS) tests, in which the frequency response of the battery cell is measured and characterized in a Nyquist plot [23–25]. The resistive behavior of the current collectors, the electrodes and the electrolyte is represented by an ohmic resistance, whose value is easily retrieved at the intersection of the curve with the real axis. At medium frequencies, one or several depressed semicircles are prominent, which are usually modeled by ZARC elements and attributed to charge transfer reactions at the electrode–electrolyte interfaces [26,27]. At low frequencies, a constant-slope tail appears, which is ascribed to diffusion processes in the electrodes and commonly represented by a CPE [28].

In order to apply fractional calculus to battery monitoring systems, a state-space representation of the fractional-order elements must be attainable and manageable, so as to implement some type of Kalman Filter (KF) to carry out the estimation of state-of-charge (SOC) as well as minimize the influence of process and measurement noises. However, fractional models involve non-integer order derivatives, which can make it challenging to obtain a practical discrete state-space formulation. A method that has become increasingly popular in the battery modeling literature in recent years relies on the Grünwald–Letnikov (GL) discretization of the fractional-order differential equation [29], thus allowing for the application of data filtering techniques. Numerous works in the past years have employed the GL definition to develop state-space representations of battery models consisting of an ohmic resistor R_0 and one or several ZARC elements, and made use of several variants of KFs to perform SOC estimations [30–32] or combined state-parameter estimations [33–36] in driving cycle experiments. This approach requires the definition of a memory of length L_m, a moving time window during which the influence of past data is still considered relevant for the computation of the fractional derivative. For this purpose, the short-memory principle presented by Podlubny [29] is applied, therefore neglecting the influence of older samples in favor of more recent data. The error ϵ introduced in the fractional derivative by the short-memory principle is quantified as in Eq. (1):

$$\epsilon \leq \frac{M L_m^{-\alpha}}{|\Gamma(1-\alpha)|} \tag{1}$$

where α is the fractional order, L_m is the memory length and M is the upper bound of the original function. Thus, given a desired degree of accuracy in the fractional derivative, the memory length L_m can be computed easily. Nevertheless, there is a caveat that is often overlooked in previous works that make use of the short-memory principle. A reduced error in the calculation of the fractional derivative can lead to an unbounded error in the output variable if the system input has been held constant for a longer period than the memory length L_m, due to the fact that the approximate derivative has already converged to zero while the exact fractional derivative is still nonzero. Consequently, the short-memory principle would only be applied accurately if the duration of the input signals were sufficiently shorter than the memory length L_m, with frequent fluctuations that cancel out long-term effects. There are several driving cycles and testing protocols that meet these conditions; however, in a real-world scenario, the input current profile cannot be known beforehand. On this account, memory lengths ranging from 10 [34] to 700 [31] have been reported in recent battery literature, revealing that there is not a consistent method to determine this value, or whether it should be variable depending on past and current operation. Despite the fact that previous works present accurate estimation results during the driving cycle stage, we consider that these aspects have not been addressed or justified rigorously. For the reasons above, a state-space representation of a fractional-order model that is able to reproduce battery behavior accurately regardless of the current profile is highly desirable.

Another alternative relies on approximating the behavior of fractional-order circuit elements by that of a combination of integer-order elements, such as resistor and capacitor networks in different configurations, for which several methods have been proposed in the literature. Oustaloup et al. [37] presented a procedure to synthesize the transfer function of the CPE by a recursive distribution of zeros and poles within a specified frequency range. Tsirimokou [38] reviewed several methods to determine rational approximations to fractional-order transfer functions and used the continued fraction expansion to calculate the parameter values of different circuit topologies. A related approach approximates the impedance of the fractional-order element by the serial connection of parallel RC branches. Farmann et al. [39] replaced the ZARC by three and five serially-connected RC elements, achieving a higher degree of accuracy with the five-element network. Kim et al. [40] also considered three RC elements. Heil and Jossen [22] proposed two methods to approximate the ZARC by multiple RC circuits: the first one consisting of an infinite number of serially connected RC elements that can be related to the ZARC by explicit equations, and the second one with only three series-connected RC circuits that requires solving a numerical minimization problem to obtain the parameter values. Authors that approximate the ZARC element by an integer-order circuit usually provide a table with the corresponding parameters for a discrete set of values of the fractional exponent α. Nevertheless, a model valid for any continuously varying order is necessary for the implementation of a Dual Fractional-Order Extended Kalman Filter (DFOEKF) for the simultaneous estimation of SOC and fractional parameters, making use of integer-order elements and avoiding the aforementioned issues regarding the memory length in the GL-based approach. We presented and discussed such a model in [41].

The main contribution of this article is the development of a novel DFOEKF for the dual estimation of SOC and fractional parameters based on the multiple-RC approximation of the ZARC element, which produces a more adequate time-domain voltage response. The fractional parameters have been identified on a novel NMC811/Si-Gr cell via both EIS tests and time-domain measurements, and the differences between both approaches as well as their suitability for this application are discussed. We have validated our novel DFOEKF procedure experimentally for 20 complete cycles including Dynamic Stress Tests (DST), rests and charging periods, also proving its robustness to incorrect parameter initializations. This method yields accurate estimation results throughout the different stages of cell operation, thus circumventing the issues that arise from the definition of a memory length when applying the GL definition of the fractional-order derivative.

Consequently, this paper is organized as follows: the theoretical analysis of different approximations of the ZARC element is presented in Section 2, whereas the experimental schemes are described in Section 3. The identification of fractional parameters from frequency-domain and time-domain data is carried out in Section 4. The novel DFOEKF method is presented and validated in Section 5, and some concluding remarks are provided in the final section.

2. Theoretical analysis

In this section, the frequency-domain and time-domain behaviors of the ZARC element are presented, and different approximations for its time-domain response are analyzed and compared.

2.1. Qualitative description of the behavior of the ZARC element in frequency and time domains

The ZARC element is composed of a constant-phase element (CPE) connected in parallel with a resistor R. The impedance of the CPE in the Laplace domain is expressed in Eq. (2):

$$Z_{CPE}(s) = \frac{1}{Qs^{\alpha}} \tag{2}$$

Therefore, the impedance of the ZARC element is presented in Eq. (3):

$$Z_{ZARC}(s) = \frac{Z_{CPE}R}{Z_{CPE}+R} = \frac{R}{1+RQs^{\alpha}} \tag{3}$$

In order to avoid fractional dimensions in parameter Q, it is useful to define a time constant as $\tau \equiv (RQ)^{1/\alpha}$ so that the final impedance is expressed in Eq. (4):

$$Z_{ZARC}(s) = \frac{R}{1+(\tau s)^{\alpha}} \tag{4}$$

The frequency response of the ZARC element can be analyzed by substituting $s = j\omega$, where $j = \sqrt{-1}$, thus obtaining Eq. (5):

$$Z_{ZARC}(j\omega) = \frac{R}{1+(j\omega\tau)^{\alpha}} = \frac{R}{1+(\omega\tau)^{\alpha}\left[\cos\left(\frac{\alpha\pi}{2}\right)+j\sin\left(\frac{\alpha\pi}{2}\right)\right]} \tag{5}$$

The impedance of the ZARC element can be split into its real and imaginary components as in Eq. (6):

$$\begin{aligned} Re(Z_{ZARC}(j\omega)) &= \frac{R\left[1+(\omega\tau)^{\alpha}\cos\left(\frac{\alpha\pi}{2}\right)\right]}{1+2(\omega\tau)^{\alpha}\cos\left(\frac{\alpha\pi}{2}\right)+(\omega\tau)^{2\alpha}} \\ Im(Z_{ZARC}(j\omega)) &= -\frac{R(\omega\tau)^{\alpha}\sin\left(\frac{\alpha\pi}{2}\right)}{1+2(\omega\tau)^{\alpha}\cos\left(\frac{\alpha\pi}{2}\right)+(\omega\tau)^{2\alpha}} \end{aligned} \tag{6}$$

The Nyquist diagram of the ZARC element, usually plotted with a negative imaginary part, features a depressed semicircle that intersects the real axis at 0 and R, which correspond to $\omega \to \infty$ and $\omega = 0$ respectively. The maximum value of the negative imaginary part is reached at $\omega = 1/\tau$ and is determined by the fractional exponent α, as expressed in Eqs. (7) and (8):

$$Re(Z_{ZARC}(j\omega))\Big|_{\omega=1/\tau} = \frac{R}{2} \tag{7}$$

$$-Im(Z_{ZARC}(j\omega))\Big|_{\omega=1/\tau} = \frac{R}{2}\frac{\sin\left(\frac{\alpha\pi}{2}\right)}{1+\cos\left(\frac{\alpha\pi}{2}\right)} = \frac{R}{2}\tan\left(\frac{\alpha\pi}{4}\right) \tag{8}$$

The time-domain voltage response of the ZARC element when the input current is a unit step can be determined via the inverse Laplace transform as in Eq. (9):

$$\begin{aligned} V_{ZARC}(s) &= I(s)Z_{ZARC}(s) = \frac{R}{s(1+(\tau s)^{\alpha})} \\ v_{ZARC}(t) &= \mathcal{L}^{-1}\left[V_{ZARC}(s)\right] = R\left(1-E_{\alpha}\left[-\left(\frac{t}{\tau}\right)^{\alpha}\right]\right) \end{aligned} \tag{9}$$

where E_{α} is the one-parameter Mittag-Leffler function, defined in Eq. (10):

$$E_{\alpha}(x) = \sum_{n=0}^{\infty}\frac{x^n}{\Gamma(n\alpha+1)} \tag{10}$$

The voltage response of the ZARC element to an arbitrary current function can be computed in Eq. (11) as in [41]:

$$v(t) = R\int_0^t i(u)\frac{d}{du}E_{\alpha}\left[-\left(\frac{t-u}{\tau}\right)^{\alpha}\right]du, \tag{11}$$

where u is a dummy variable. Therefore, if the current profile is approximated by a piecewise constant function, the exact voltage response of the ZARC element can be computed as in Eq. (12):

$$v_{ZARC}(t) = R\sum_{m=1}^{k} I_m\left[\left(1-E_{\alpha}\left[-\left(\frac{t-t_m}{\tau}\right)^{\alpha}\right]\right)H(t-t_m) - \left(1-E_{\alpha}\left[-\left(\frac{t-t_{m-1}}{\tau}\right)^{\alpha}\right]\right)H(t-t_{m-1})\right] \tag{12}$$

where H is the Heaviside unit step function.

Table 1
Parameter expressions as a function of α for the 5 RC approximation. [41].

Parameter	Expression
$r_1(\alpha) = r_5(\alpha)$	$0.186(1-\alpha)^{1.1}$
$r_2(\alpha) = r_4(\alpha)$	$(0.25+0.57\alpha^2)(1-\alpha)^{0.72}$
$r_3(\alpha)$	$1-2\left(r_1+r_2\right)$
$t_1(\alpha) = 1/t_5(\alpha)$	$\frac{0.045\alpha^{7.32}}{0.04+\alpha^{4.47}}$
$t_2(\alpha) = 1/t_4(\alpha)$	$\frac{0.407\alpha^{4}}{0.071+\alpha^{2.38}}$
$t_3(\alpha)$	1

Table 2
Parameter expressions as a function of α for the 7 RC approximation. [41].

Parameter	Expression
$r_1(\alpha) = r_7(\alpha)$	$0.14(1-\alpha)^2$
$r_2(\alpha) = r_6(\alpha)$	$0.22(1-\alpha)-0.08(1-\alpha)^3$
$r_3(\alpha) = r_5(\alpha)$	$\left(0.12+0.057e^{3.4\alpha}\right)(1-\alpha)$
$r_4(\alpha)$	$1-2\left(r_1+r_2+r_3\right)$
$t_1(\alpha) = 1/t_7(\alpha)$	$1.4\cdot 10^{-8}e^{19\alpha(1.6-\alpha)}$
$t_2(\alpha) = 1/t_6(\alpha)$	$\frac{0.078\alpha^{5.63}}{0.026+\alpha^{3.67}}$
$t_3(\alpha) = 1/t_5(\alpha)$	$\frac{0.56\alpha^{2.27}}{0.4+\alpha^{1.3}}$
$t_4(\alpha)$	1

2.2. Time-domain approximations of the ZARC element

The exact calculation of the ZARC voltage response with Eq. (12) requires the repeated computation of the Mittag-Leffler function, which is iterative in nature itself. This results in a heavy computational load, thus making it not easily applicable in real-time monitoring algorithms. Consequently, several time-domain implementations have been proposed in order to accurately approximate the voltage response of the ZARC element in the time domain.

- Multiple-RC approximation. This approach relies on approximating the frequency response of the ZARC element by that of a set of series-connected parallel RC branches. Taking the fractional order α, the resistance R_{ZARC} and the time constant τ_{ZARC} as the three input parameters of the ZARC model, the parameter values are directly calculated as $R_i = R_{ZARC}\cdot r_i(\alpha)$ and $\tau_i = \tau_{ZARC}\cdot t_i(\alpha)$ for both the five-element and seven-element networks according to Tables 1 and 2 [41]:
Once the equivalent RC parameter values have been calculated, the state-space representation of a set of series-connected parallel RC branches is shown in Eq. (13):

$$\begin{aligned} &x(k) = Ax(k-1)+Bu(k-1), \qquad y(k) = Cx(k)+Du(k) \\ &x(k) = \begin{bmatrix} i_1(k) & i_2(k) & \dots & i_n(k)\end{bmatrix}^T \end{aligned} \tag{13}$$

where the state vector x contains the currents through each resistor, the input u is the total current and the output y is the total voltage drop in the network. The state-space representation matrices are expressed in Eq. (14):

$$\begin{aligned} A &= diag\left[\exp\left(-\frac{\Delta t}{\tau_1}\right) \quad \exp\left(-\frac{\Delta t}{\tau_2}\right) \quad \dots \quad \exp\left(-\frac{\Delta t}{\tau_n}\right)\right] \\ B &= \left[1-\exp\left(-\frac{\Delta t}{\tau_1}\right) \quad 1-\exp\left(-\frac{\Delta t}{\tau_2}\right) \quad \dots \quad 1-\exp\left(-\frac{\Delta t}{\tau_n}\right)\right]^T \\ C &= \begin{bmatrix} R_1 & R_2 & \dots & R_n\end{bmatrix}, \qquad D = 0 \end{aligned} \tag{14}$$

where Δt is the sampling time.

- Oustaloup approximation. This method first approximates the frequency response of a constant-phase element of order α in a certain frequency range $[\omega_l, \omega_h]$ by a product of n zeroes and poles as in Eq. (15):

$$Z_{CPE}(s) = \frac{1}{\left(\frac{s}{\omega_c}\right)^{\alpha}} \approx \left(\frac{\omega_c}{\omega_l}\right)^{\alpha} \prod_{h=-N}^{N} \frac{1+\frac{s}{\omega_{z,h}}}{1+\frac{s}{\omega_{p,h}}} \equiv Z_{OU}(s) \tag{15}$$

where $\omega_c = \sqrt{\omega_l \omega_h}$ and $N = \frac{n-1}{2}$. The corresponding zeroes and poles are calculated in Eq. (16):

$$\omega_{z,h} = \omega_l \left(\frac{\omega_h}{\omega_l}\right)^{\frac{h+\frac{n+\alpha}{2}}{n}}, \omega_{p,h} = \omega_l \left(\frac{\omega_h}{\omega_l}\right)^{\frac{h+\frac{n-\alpha}{2}}{n}} \tag{16}$$

Adding a parallel resistor R yields a biproper transfer function, which can be further split into the sum of a direct term R_0 and n first-order partial fractions as in Eq. (17), where the new poles are $[1/\tau_1, 1/\tau_2, \ldots, 1/\tau_n]$ and the residues are $[R_1, R_2, \ldots, R_n]$:

$$Z_{ZARC,OU}(s) = R_0 + \frac{R_1}{1+\tau_1 s} + \frac{R_2}{1+\tau_2 s} + \cdots \frac{R_n}{1+\tau_n s} \tag{17}$$

This equation leads to a state-space representation similar to that of Eqs. (13) and (14), with the difference that the feedthrough matrix D is now equal to R_0 in this case. This entails a slight inaccuracy in the Oustaloup model in relation to the multiple-RC model as it introduces a direct term from the input to the output that is not present in the expression for the theoretical voltage in Eq. (12). This discrepancy translates into a voltage leap when current is changed along with a small steady-state error when current has been held constant for a long period of time.

It has to be noted that the accuracy of the approximation depends heavily both on the number of zeroes and poles n and the frequency range $[\omega_l, \omega_h]$ considered. From now on, in this article the operational range will be set to $[10^{-3}\tau, 10^{3}\tau]$, as it provides a good compromise between time-domain and frequency-domain accuracy [41].

- Grünwald–Letnikov approximation. This method, rather than approximating the frequency response of the ZARC element, relies on discretizing the underlying fractional-order differential equation for the current through the ZARC resistor, shown in Eq. (18):

$$D^{\alpha} i_{R,ZARC}(t) = -\frac{1}{\tau^{\alpha}} i_{R,ZARC}(t) + \frac{1}{\tau^{\alpha}} I(t) \tag{18}$$

where $I(t)$ is the input current.

This is achieved by introducing the Grünwald–Letnikov (GL) definition of the fractional derivative with a fixed memory length L_m [29], as in Eq. (19):

$$D^{\alpha} x(k+1) = \frac{1}{T_s^{\alpha}} \sum_{j=0}^{L_m} (-1)^j \binom{\alpha}{j} x(k+1-j) \tag{19}$$

which renders the state Eq. (20) when substituted into Eq. (18):

$$i_{R,ZARC}(k+1) = \left(\alpha - \frac{T_s^{\alpha}}{\tau^{\alpha}}\right) i_{R,ZARC}(k) + \sum_{j=2}^{L_m} (-1)^{j+1} \binom{\alpha}{j} i_{R,ZARC}(k+1-j) \tag{20}$$

If a vector containing previous values of $i_{R,ZARC}$ is considered as a state vector, Eq. (20) can be expressed more compactly in matrix form as in Eq. (21) [33]:

$$x(k+1) = Ax(k) + Bu(k) \quad y(k) = Cx(k) + Du(k) \tag{21}$$

where

$$x(k) = \begin{bmatrix} i_{R,ZARC}(k) & i_{R,ZARC}(k-1) & \ldots & i_{R,ZARC}(k-L+1) \end{bmatrix}^T$$

$$A = \begin{bmatrix} \alpha - \frac{T_s^{\alpha}}{\tau^{\alpha}} & W_2 & W_3 & \ldots & W_{L_m} \\ 1 & 0 & 0 & \ldots & 0 \\ 0 & 1 & 0 & \ldots & 0 \\ \vdots & \vdots & \vdots & \ddots & \vdots \\ 0 & 0 & \ldots & 1 & 0 \end{bmatrix}, B = \begin{bmatrix} \frac{T_s^{\alpha}}{\tau^{\alpha}} \\ 0 \\ 0 \\ \vdots \\ 0 \end{bmatrix}$$

$$C = \begin{bmatrix} R & 0 & 0 & \ldots & 0 \end{bmatrix}, D = 0, W_j = \binom{\alpha}{j} \tag{22}$$

2.3. Accuracy comparison between the time-domain approximations

In order to elucidate which method provides the most accurate approximation of the voltage response of the ZARC element, each one has to be compared to the exact result. Agudelo et al. [42] recently presented a comparison of three time-domain implementations of fractional impedance models for several arbitrary values of the input parameters R_{ZARC}, τ_{ZARC} and α; however, here a more systematic approach is taken by employing a normalized resistance and a wider range of both τ_{ZARC} and α, covering most typical values of the fractional order exponent α and time constant τ_{ZARC}. For this purpose, a current profile characteristic of battery operation, consisting of one normalized DST cycle (assuming a constant operating battery voltage) and one constant-current charging period, is simulated for $0.5 < \alpha < 0.9$ and for $\tau_{ZARC} = 20$ s, $\tau_{ZARC} = 100$ s and $\tau_{ZARC} = 500$ s with a unit resistance and a sampling time $T_s = 1$ s, as shown in Fig. 1.

The relative RMS error between the exact voltage response and each approximation is computed. Simulation results for the 5RC and 7RC approximations for the multiple-RC and Oustaloup methods are shown in Figs. 2 and 3, whereas errors for the GL approach are depicted in Fig. 4.

The overall satisfactory operation of the first two methods can be observed in Figs. 2 and 3, with relative errors below the 5% threshold in almost all cases and greater accuracy as α increases. However, it has to be pointed out that the multiple-RC method yields a slightly smaller voltage error and ensures a more consistent performance regardless of the value of the time constant τ_{ZARC}. Furthermore, the accuracy of both approximations improves roughly by a factor of two when the number of RC elements is increased from 5 to 7.

Finally, the relative error between the exact voltage and the one obtained with the GL method for memory lengths $L_m = 50$ and $L_m = 500$ is displayed in Fig. 4. It can be easily ascertained that this is the least effective of the three approaches for the fractional modeling of LIBs since its accuracy depends heavily on the value of the time constant τ_{ZARC} due to the effect of the limited memory length. Even at the best-case scenario for the longest memory and the smallest time constant ($\tau_{ZARC} = 20$ s and $L_m = 500$), the RMS error is still higher than that of both earlier approximations for 5 RC elements. This shows that the number of states in the GL approach should be at least two orders of magnitude higher than in the multiple-RC and Oustaloup methods for a similar degree of accuracy if the complete operation of the battery is taken into account.

A qualitative example of this behavior can be observed in Fig. 5. Throughout the DST discharge cycle there are quick changes in current, which allow the GL approximation to remain as accurate as the other two. However, during rest periods and constant-current phases the shortcomings of the GL approach become apparent as the limited memory length causes the voltage to converge to its steady-state value in an excessively fast manner. This issue may not seem critical when it comes to rests as the steady-state value is zero and the only difference is the rate at which it is reached. Nevertheless, in constant-current charging phases the steady-state value is not zero (for example, it is

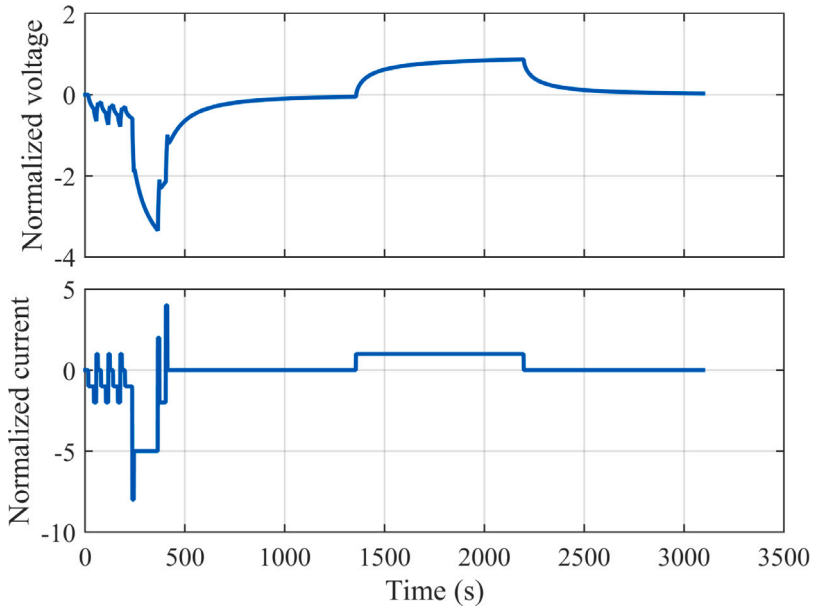

Fig. 1. Normalized input current and exact voltage response for $\alpha = 0.65$ and $\tau_{ZARC} = 100$ s.

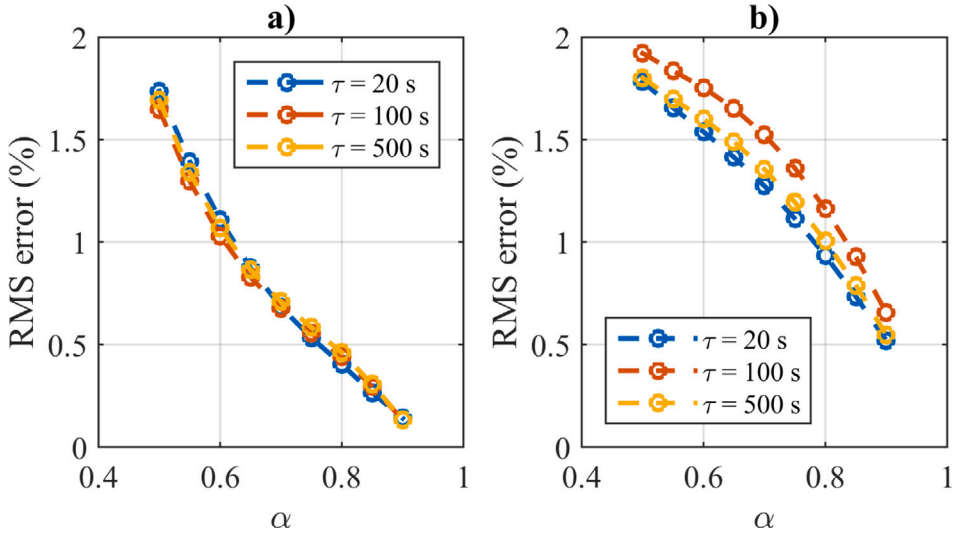

Fig. 2. RMS error comparison for a 5RC approximation between (a) Multiple-RC approach, and (b) Oustaloup approach.

1 in Fig. 5), which leads to a substantial steady-state error that may result in prolonged incorrect state-of-charge estimations. This raises a valid concern whether or not the GL approximation is appropriate for online battery monitoring given that rests and constant-current charges make up the majority of the total operation time. This could also have a knock-on effect on online state-of-health (SOH) estimations if the remaining capacity is estimated directly or indirectly from the quotient $\Delta Q/\Delta SOC$ [43,44]. Additionally, the higher computational and memory requirements for the GL approach might be an issue for an on-board implementation.

Both the multiple-RC and the Oustaloup approaches yield reasonably satisfactory results, with the proposed multiple-RC being slightly more accurate. Therefore, in the rest of this article, only the multiple-RC approach with seven RC elements will be further used.

3. Experimental

The experimental tests were conducted on a high-energy silicon–graphite, nickel rich commercial cell manufactured by Samsung-SDI (INR18650-35E). According to the manufacturer, this type of cell exhibits a standard discharge capacity greater or equal than 3350 mAh when discharged at C/2 within the voltage limits (i.e., 4.2 V charge, 2.65 V cut-off). The experimental cycling testing was carried out on a multichannel, high-precision series Arbin LBT battery tester. For the EIS experiments, a Gamry Reference 3000™ high-performance potentiostat/galvanostat was employed. A Memmert environmental chamber was used throughout the experimental procedures to maintain a constant ambient temperature of 23 °C.

The battery testing strategy is based on the established testing schemes developed at the United States Advanced Battery Consortium (USABC) [45] and on the best practices for battery testing developed at the Hawaii Natural Energy Institute (HNEI) [46]. The tests began with the conditioning procedures following the USABC guidelines [45], with and added thermodynamic C/25 cycling following HNEI recommendations [46]. This set of testing allows for the determination of the pseudo Open Circuit Voltage (OCV) curve to decipher the OCV-SOC relationship.

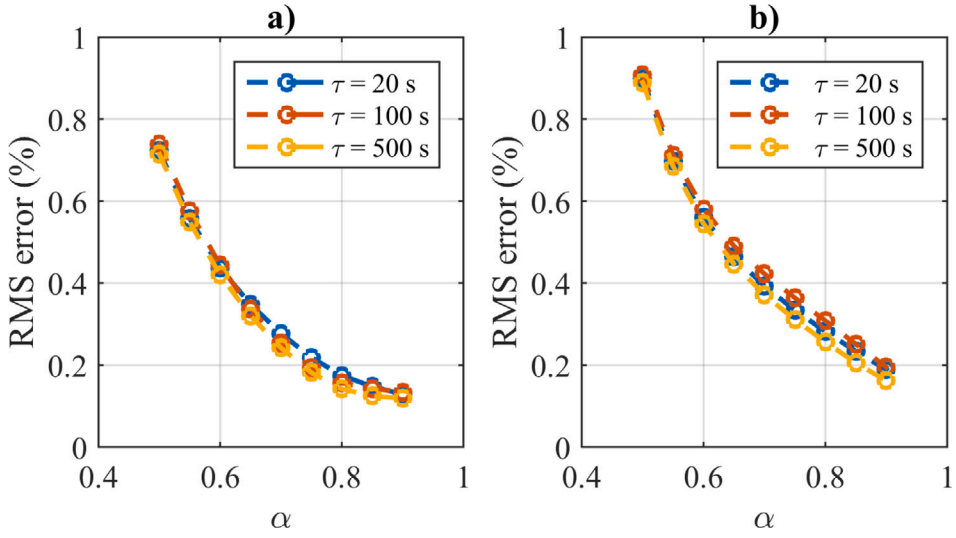

Fig. 3. RMS error comparison for a 7RC approximation between (a) Multiple-RC approach, and (b) Oustaloup approach.

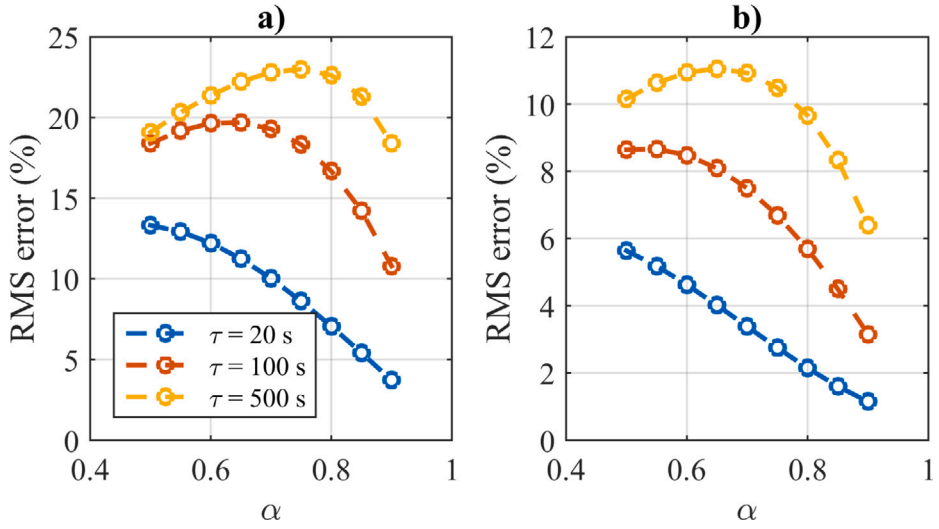

Fig. 4. RMS error comparison between (a) $L_m = 50$ (b) $L_m = 500$ for the GL approach.

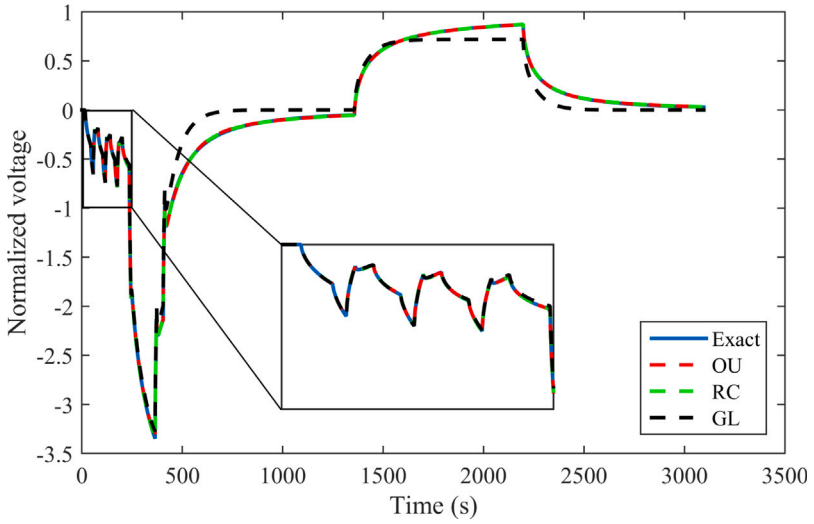

Fig. 5. Normalized voltage responses for $\alpha = 0.65$, $\tau_{ZARC} = 100$ s, with 7 RC elements for the Oustaloup and multiple-RC approximations and $L_m = 100$ for the GL approximation.

Thereafter, a Reference Performance Test (RPT) was performed. RPTs quantitatively assess battery performance using standard testing equipment, providing as much information as possible without being intrusive. In particular, this RPT started with a set of charge and discharge cycles at different discharge rates, while maintaining the charging procedure. The charging method followed the standard scheme at constant current–constant voltage (CC–CV) at C/2 (1.7 A) to 4.2 V until the current decreased to C/50 (67 mA), while the discharging rates were 1C, C/2 and C/5, respectively. Following this set of charge/discharge cycles, a thermodynamic cycle at C/25 was carried out. To conclude the RPT, the EIS experiments were performed in a frequency range from 10 mHz to 10 kHz at the following states of charge: 5%, 20%, 50%, 80% and 95%.

Once the RPTs were completed, the continuous Duty Cycling Scheme (DCS) was carried out. The DCS testing consisted of a set of standard charge (CC–CV) at C/2 to 4.2 V, followed by DST profiles as defined by the USABC manual [45]. The DST is a variable-power discharge regime developed by the USABC to simulate the expected demands of an EV battery. The DST schedule was scaled to 700 W/kg, surpassing the long-term USABC power goal of 400 W/kg. The resulting maximum C-rates during the DST charge and discharge pulses were approximately 2.6 A (0.75C) and 12 A (3.5C), respectively, with an average rate corresponding to a C/2 discharge. The average energy throughput per full discharge was approximately 10 Wh. The DST schedule was repeated every 360 s until the cell reached its discharge cut-off voltage of 2.65 V, after which the cell was set to rest for 2 h. The standard CC–CV charge-DST discharge cycling procedure was performed continuously for 20 cycles in succession.

4. Identification of ZARC parameters

In this section, the identification of fractional parameters is carried out from experimental frequency-domain and time-domain data, and the differences between both approaches as well as their suitability and applications are discussed.

4.1. Frequency-domain identification

In order to identify fractional parameters from frequency-domain data, it has to be pointed out that in most experimental EIS measurements, the leftmost depressed semicircle is usually prominent; the constant-slope behavior at lower frequencies is not as easily identifiable nonetheless. Moreover, the fact that batteries present a bounded DC impedance is an additional reason to use a multiple-ZARC equivalent circuit model to fit EIS data, as shown in Fig. 6.

In order to fit our experimental data, we will use the equivalent circuit model depicted in Fig. 7, comprised of one series resistor R_0 and 3 ZARC elements.

The parameterization was carried out with Particle Swarm Optimization (PSO), which is a widespread population-based optimization algorithm often employed for the concurrent identification of multiple parameters [47]. It is a well-documented algorithm, summarized as follows: a collection of individuals (particles) moves in steps throughout a bounded n-dimensional search area, where n is the number of parameters to be optimized. At each step, the algorithm evaluates the objective function at each particle. The new velocity of each particle is updated according to the cost function, the individual best location and the global best location. If the upper and lower bounds define a region with one global minimum, the population will eventually coalesce around this location.

In this case, the cost function is the weighted squared distance in the Nyquist plot between the experimental and the estimated impedances Z_{exp} and Z_{est} at every frequency point, expressed in Eq. (23):

$$C = \sum_{k=1}^{N} w_k \left[\left(Im(Z_{est}(j\omega_k)) - Im(Z_{exp}(j\omega_k)) \right)^2 + \left(Re(Z_{est}(j\omega_k)) - Re(Z_{exp}(j\omega_k)) \right)^2 \right] \quad (23)$$

Weights w_k are introduced so as to penalize errors at lower frequencies in a harsher way, since a precise parameterization of the frequency response in this range is critical to accurately reproduce cell behavior at longer timescales. Experimental and fitted data are shown in Figs. 8 and 9, along with the lower and upper frequency limits and the frequency of the valley that is characteristic of EIS plots. It has to be noted that the minor discrepancies between experimental and fitted points in the high frequency limit are not caused by a modeling error, but they are due to parasitic inductive elements that make the experimental curve intersect the real axis at a much lower frequency than the theoretical limit $\omega \to \infty$ [24].

Fitted parameters for the five analyzed SOCs are shown in Table 3.

Table 3
Summary of identified ZARC parameters from EIS measurements.

Parameters	SOC = 5%	SOC = 20%	SOC = 50%	SOC = 80%	SOC = 95%
$R_0(\Omega)$	0.023	0.02313	0.0231	0.02313	0.02324
$R_1(\Omega)$	0.0118	0.0064	0.0053	0.0056	0.0061
$\tau_1(s)$	0.0038	0.0013	0.0011	0.0011	0.0014
α_1	0.5273	0.7302	0.7682	0.7416	0.7080
$R_2(\Omega)$	0.0072	0.0057	0.0074	0.0050	0.0069
$\tau_2(s)$	1.9146	1.5780	1.9051	1.2407	1.9501
α_2	0.6722	0.7136	0.7150	0.6844	0.6140
$R_3(\Omega)$	0.1987	0.0751	0.0788	0.0592	0.0678
$\tau_3(s)$	195.65	148.04	132.04	161.57	167.02
α_3	0.8507	0.8216	0.8152	0.7207	0.7439

4.2. Time-domain identification

Several methods for the time-domain identification of fractional impedance parameters have been proposed based on the GL definition of the fractional derivative. For this purpose, a characteristic current profile is introduced as an input and the voltage response is recorded. Afterwards, said voltage response is adjusted to that of an equivalent circuit model, and the identified parameters are those which minimize the voltage error along the duration of the experiment. Solomon et al. [32] used both PSO and QPSO (Quantum Particle Swarm Optimization) in order to determine four equivalent circuit parameters for the entire SOC range from driving cycle data. Hu et al. [34] employed a hybrid GA-PSO (Genetic Algorithm-Particle Swarm Optimization) to simultaneously identify the equivalent circuit parameters and the polynomial coefficients of the OCV-SOC relationship, whereas He et al. [31] employed an adaptive GA-based method. Despite the acceptable agreement between the experimental and the simulated responses to the respective current profiles, the ZARC resistance values are greater than 1 Ω in [34] and less than 1 mΩ in [31], whereas the obtained fractional-order exponents are extremely close to 1 in [48], which poses a question about the validity of these parameters in a different setting.

This emphasizes the relevance of EIS tests for informed time-domain parameter identification as they provide illustrative values that can be useful to narrow down the search space for the optimization algorithm, since some error minima may result in parameter values that are not physically meaningful. On this account, Mawonou et al. [33] used the results from frequency domain identification from EIS tests to initialize a RLS algorithm with a forgetting factor for a faster convergence of the time-domain identification from both current pulse excitations and driving cycle data. In our case, 24 DST cycles were carried out in succession in order to cover a full discharge from the high to the low cutoff voltages. To this end, the amplitude spectrum of 24 consecutive ideal and normalized DST profiles assuming a constant operating battery voltage is computed and shown in Fig. 10.

It is observed that frequency components greater than 0.1 Hz have an amplitude less than 0.1. This means that time constants below

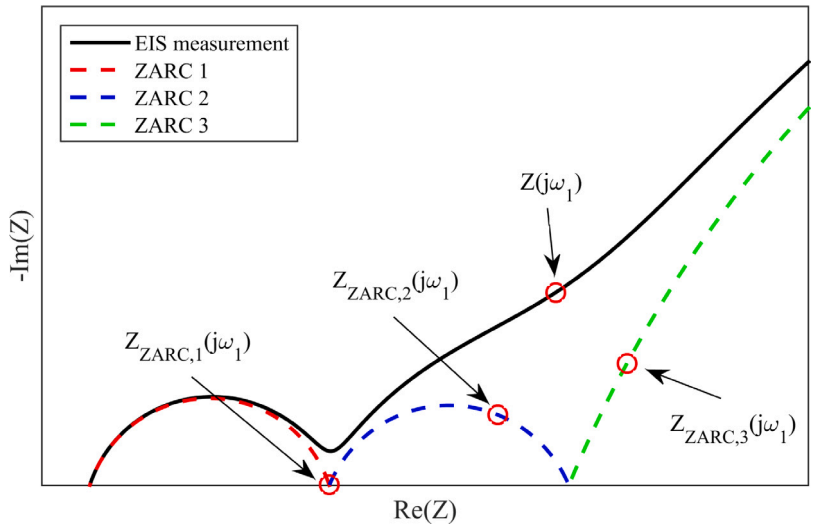

Fig. 6. Qualitative examples of ZARC identification in EIS measurements. Red circles show the contribution of each ZARC element to the total impedance. Note that each Z element has been displaced in the X direction for convenience.

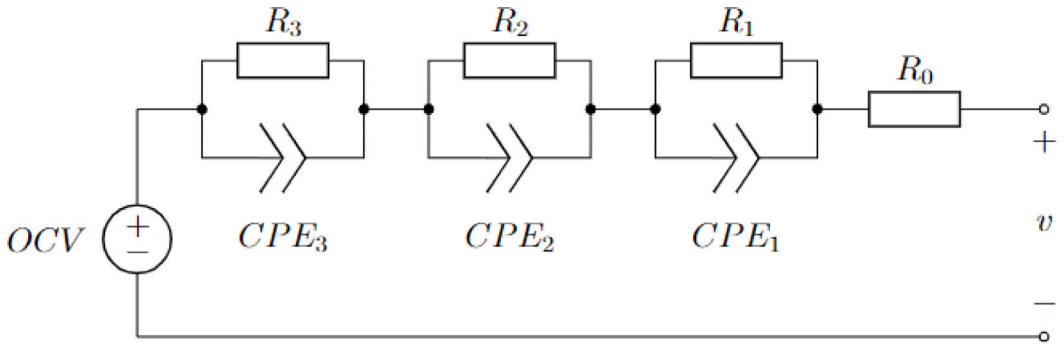

Fig. 7. Equivalent circuit model.

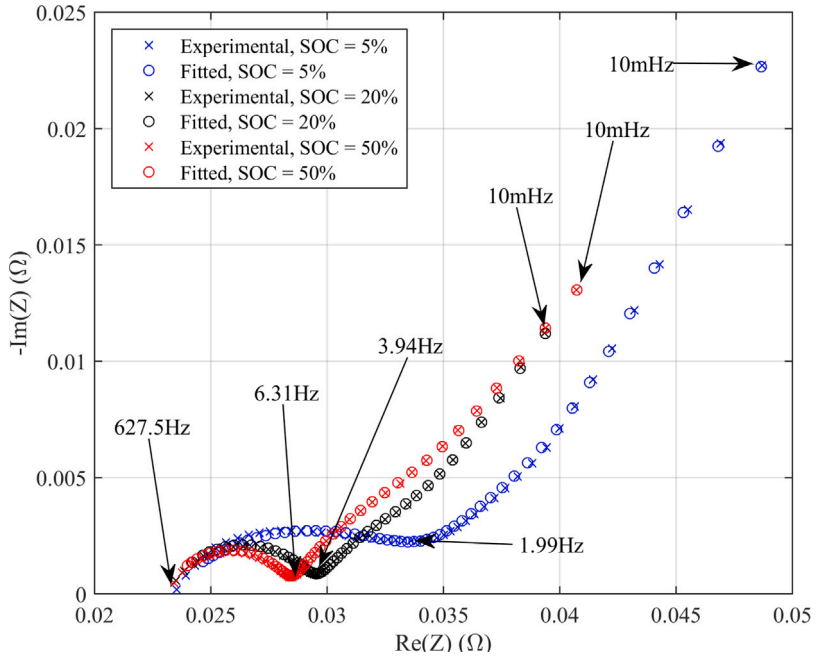

Fig. 8. EIS experimental measurements and fitted values for SOC = 5%, SOC = 20% and SOC = 50%.

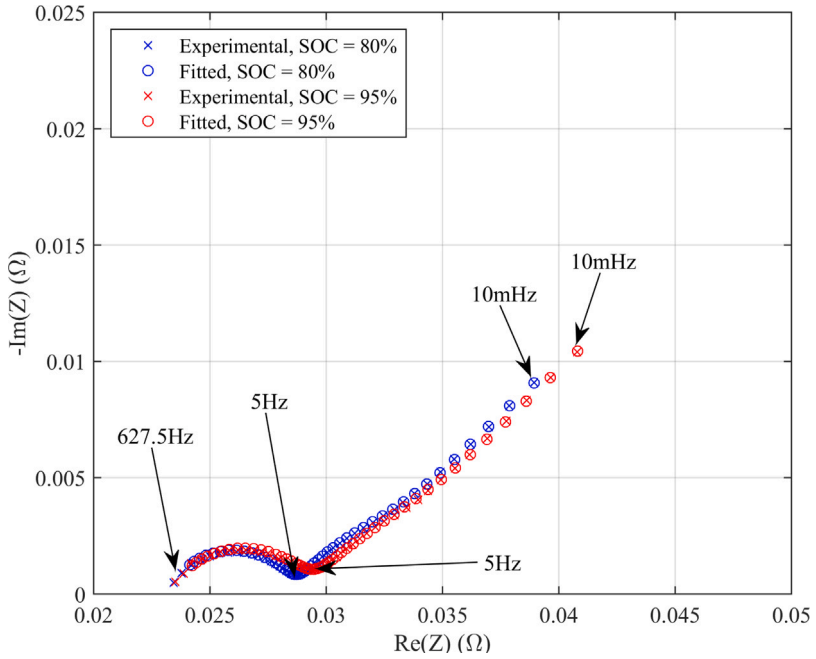

Fig. 9. EIS experimental measurements and fitted values for SOC = 80% and SOC = 95%.

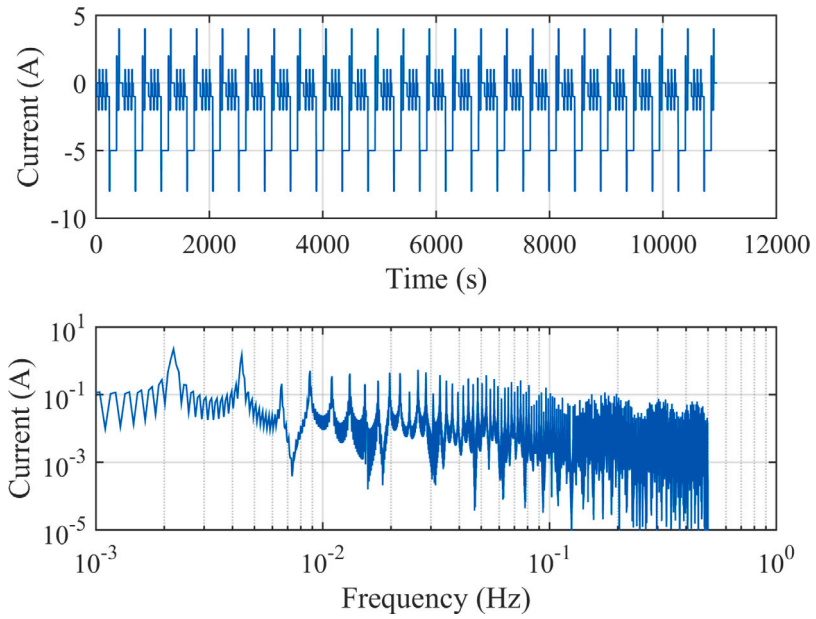

Fig. 10. Ideal amplitude spectrum of the repeated DST current profile.

1.59 s will be difficult to identify from the voltage response to this current profile. In particular, this implies that the two ZARC elements in Fig. 7 with faster time constants τ_1, τ_2 will not be detected properly. Therefore, an equivalent circuit model with a voltage source with the OCV-SOC relationship determined in Section 3 and an impedance consisting of a series resistor and a ZARC element will be employed in this section and four parameters $(R_0, R_{ZARC}, \tau_{ZARC}, \alpha)$ will be identified from time-domain measurements. Carrying out this analysis prior to the time-domain identification proves to be essential for an informed parameterization, since an unrestricted optimization procedure from only time-domain measurements may lead to overfitting. For instance, issues such as identifying two ZARC elements with similar time constants [30,31,34] or even three ZARC elements from driving cycle data [49] can be easily avoided.

Standard Particle Swarm Optimization is employed again, with the cost function being the RMS error between the measured voltage and the simulated voltage according to the state-space representation in Eqs. (13) and (14). Parameter values for ZARC 3 in Table 3 were used as guidelines to set the upper and lower boundaries for the search space. The convenience of the expressions in Table 2 becomes apparent as they provide the parameter values for the multiple-RC approximation directly, without the need for repeating the pole-zero decomposition procedure and residue calculation in every iteration of the minimization algorithm. The identified parameters are: $R_0 = 0.0250$ Ω, $R_{ZARC} = 0.0627$ Ω, $\tau_{ZARC} = 247.25$ s, $\alpha = 0.5038$, with an RMS error of 11.9 mV. The accurate match between the measured and simulated voltage, along with the current input, are shown in Fig. 11.

Both time-domain responses are shown in Fig. 12 for a complete DST cycle with an RMS error of 11.9 mV for the time-domain identified

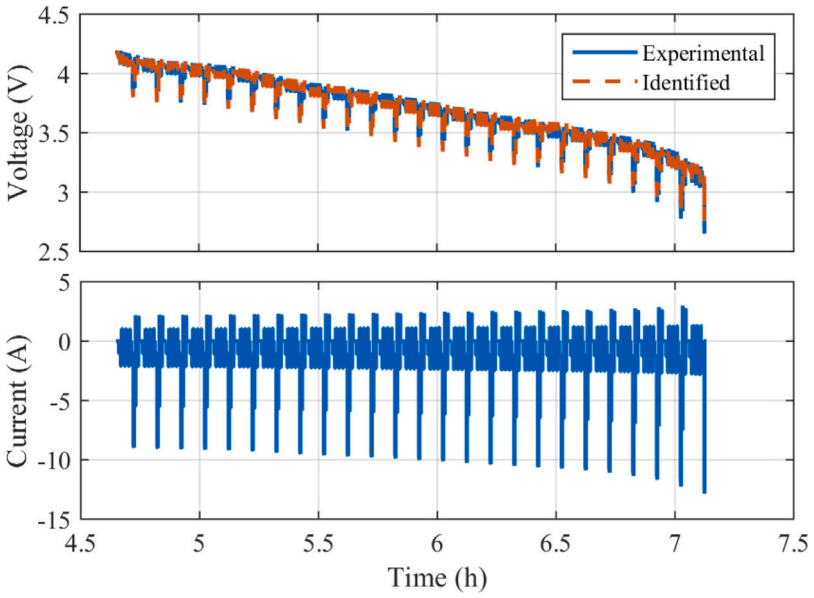

Fig. 11. Experimental and simulated voltage with the parameter values identified from time-domain measurements. It has to be noted that as the battery discharges and its operational voltage decreases, the current must increase to meet the constant power demand.

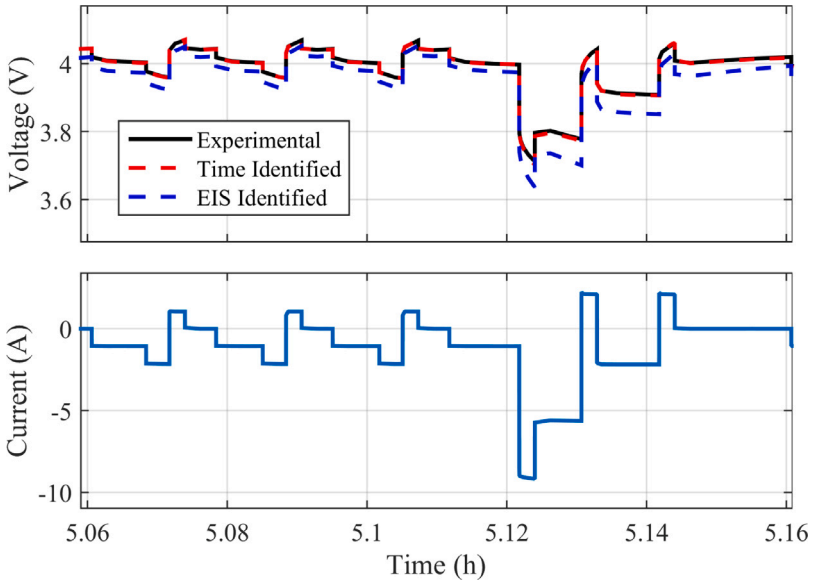

Fig. 12. Experimental and simulated voltage with the parameter values identified from time-domain measurements and EIS measurements. Detail of a single DST cycle.

parameters and 39.3 mV for the frequency-domain identified parameters. It is noted that while the former closely matches the measured voltage, the latter presents an additional voltage drop due to the higher resistance identified in EIS tests. This could be due to the non-linear current dependence of charge-transfer processes, which may cause resistance values identified at lower currents to be greater than those identified at higher current rates. Therefore, further research on the development of more complex ECMs is warranted in order to account for the nonlinear behavior of lithium-ion batteries.

This goes to show that frequency-domain parameters, although a guideline for the time-domain identification procedure, may not be the best option for time-domain simulation and monitoring given the non-linearity of battery voltage response with the input current amplitude if the current dependence of charge-transfer processes is not explicitly taken into account in the equivalent circuit model [50,51].

5. Dual estimation of SOC and fractional parameters

Similarly, several methods for the online estimation of SOC and equivalent circuit parameter values based on fractional models have been proposed based on the GL definition of the fractional derivative. The interest in detecting and estimating changes in the equivalent circuit elements is justified by the variations in parameter values observed in EIS tests at different states of charge and stages of degradation. Hu et al. [34] employed a fractional-order Dual Extended Kalman Filter to coestimate battery capacity Q and series resistance R_0, although it was intended as a method to correct the erroneous initialization of these

parameters rather than a procedure for long-term estimation. Mawonou et al. [33] combined an Extended Kalman Filter for SOC estimation with a Recursive Least Squares algorithm with a forgetting factor to estimate the series resistance R_0 and the ZARC resistance and time constant R_{ZARC}, τ_{ZARC}. Yu et al. [36] presented a CPSO-based algorithm for online parameter identification, and showed that the convergence time as well as the identification results depend heavily on the memory length and the tuning parameters.

However, as shown in Section 2, the GL approximation is not the most appropriate for accurate battery fractional modeling outside the driving cycle stage; therefore, the validity of these methods is not guaranteed in prolonged operation containing rests and constant-current charging periods. For this reason, a novel method for the long-term simultaneous estimation of battery SOC and all fractional parameters based on the multiple-RC approximation presented in Section 2 is described next.

5.1. Proposed DFOEKF

In this section, the proposed method will be presented assuming an equivalent circuit model consisting of a voltage source representing the OCV-SOC relationship determined in Section 3, one series resistor R_0 and one ZARC element with parameters $R_{ZARC}, \tau_{ZARC}, \alpha$, although the method could be easily extended for several ZARC elements. The state and output equations are the expressed in Eqs. (24) and (25):

$$
\begin{aligned}
&x(k) = Ax(k-1) + Bu(k-1)\\
&x(k) = \begin{bmatrix} SOC(k) & i_1(k) & i_2(k) & \dots & i_7(k) \end{bmatrix}^T, \qquad u(k) = i(k)\\
&A = diag\left[1 \quad \exp\left(-\tfrac{\Delta t}{\tau_1}\right) \quad \exp\left(-\tfrac{\Delta t}{\tau_2}\right) \quad \dots \quad \exp\left(-\tfrac{\Delta t}{\tau_7}\right)\right]\\
&B = \left[\tfrac{\Delta t}{Q} \quad 1-\exp\left(-\tfrac{\Delta t}{\tau_1}\right) \quad 1-\exp\left(-\tfrac{\Delta t}{\tau_2}\right) \quad \dots \quad 1-\exp\left(-\tfrac{\Delta t}{\tau_7}\right)\right]^T
\end{aligned}
\tag{24}
$$

$$
v_k = OCV(SOC_k) + R_0 i_k + R_1 i_{1,k} + R_2 i_{2,k} + \cdots + R_7 i_{7,k} \tag{25}
$$

The Dual Extended Kalman Filter (DEKF) consists of two EKFs in a parallel configuration for simultaneous estimation of both states and parameters, whose general formulation is described in Eq. (26):

$$
\begin{aligned}
x_k &= f(x_{k-1}, u_{k-1}, \theta_k) + w_k\\
y_k &= h(x_k, u_k, \theta_k) + v_k\\
\theta_k &= \theta_{k-1} + r_k\\
d_k &= h(x_k, u_k, \theta_k) + e_k
\end{aligned}
\tag{26}
$$

where x_k is the state vector, u_k is the model input, θ_k is the vector containing the parameters to be estimated and y_k is the model output. f and h are non-linear functions that update the current state and output, and w_k and v_k are the zero-mean process and measurement noises of covariance Q_k^x and R_k^x, respectively. Given that model parameters are assumed to change in a much slower fashion compared to state dynamics, their fluctuations are attributed to noise r_k with covariance Q_k^θ. The parameter output equation d_k is the same as the state output equation, with noise e_k of covariance R_k^θ.

Following state and parameter initialization, the operation of the DEKF can be summarized in four steps in Eqs. (27), (28), (30) and (32), respectively:

1. **Parameter EKF estimation.**

$$
\begin{aligned}
\hat{\theta}_k^- &= \hat{\theta}_{k-1}^+\\
P_{\theta,k}^- &= P_{\theta,k-1}^+ + Q_k^\theta
\end{aligned}
\tag{27}
$$

2. **State EKF estimation.**

$$
\begin{aligned}
\hat{x}_k^- &= f(\hat{x}_{k-1}^+, u_{k-1}, \hat{\theta}_k^-)\\
P_{x,k}^- &= F_{k-1}^x P_{x,k-1}^+ \left(F_{k-1}^x\right)^T + Q_k^x\\
\hat{y}_k &= h(\hat{x}_k^-, u_k, \hat{\theta}_k^-)
\end{aligned}
\tag{28}
$$

where

$$
F_{k-1}^x = \left.\frac{\partial f(x_{k-1}, u_{k-1}, \hat{\theta}_k^-)}{\partial x_{k-1}}\right|_{x_k = \hat{x}_{k-1}^+} \tag{29}
$$

3. **State EKF correction.**

$$
\begin{aligned}
L_k^x &= P_{x,k}^- \left(H_k^x\right)^T \left(H_k^x P_{x,k}^- \left(H_k^x\right) + R_k^x\right)\\
\hat{x}_k^+ &= \hat{x}_k^- + L_k^x \left(y_k - \hat{y}_k\right)\\
P_{x,k}^+ &= \left(I - L_k^x H_k^x\right)^T P_{x,k}^- \left(I - L_k^x H_k^x\right) + L_k^x R_k^x \left(L_k^x\right)^T
\end{aligned}
\tag{30}
$$

where

$$
H_k^x = \left.\frac{\partial h(x_k, u_k, \hat{\theta}_k^-)}{\partial x_k}\right|_{x_k = \hat{x}_k^-} \tag{31}
$$

4. **Parameter EKF correction.**

$$
\begin{aligned}
L_k^\theta &= P_{\theta,k}^- \left(H_k^\theta\right)^T \left(H_k^\theta P_{\theta,k}^- \left(H_k^\theta\right) + R_k^\theta\right)\\
\hat{\theta}_k^+ &= \hat{\theta}_k^- + L_k^\theta \left(d_k - \hat{d}_k\right)\\
P_{\theta,k}^+ &= \left(I - L_k^\theta H_k^\theta\right)^T P_{\theta,k}^- \left(I - L_k^\theta H_k^\theta\right) + L_k^\theta R_k^\theta \left(L_k^\theta\right)^T
\end{aligned}
\tag{32}
$$

where

$$
H_k^\theta = \left.\frac{dh(\hat{x}_k, u_k, \theta_k)}{d\theta_k}\right|_{\theta_k = \hat{\theta}_k^-} \tag{33}
$$

The corrected error covariance matrices are expressed in Joseph form to improve the numerical stability of the algorithm [52]. It has to be pointed out that the calculation of matrix H_k^θ requires the computation of the total differential of the model output equation with respect to parameters. For this reason, the total derivative has to be decomposed into partial derivatives as in Eqs. (34) and (35):

$$
H_k^\theta = \left.\frac{dh(\hat{x}_k, u_k, \theta_k)}{d\theta_k}\right|_{\theta_k = \hat{\theta}_k^-} = \frac{\partial h(\hat{x}_k, u_k, \hat{\theta}_k^-)}{\partial \hat{\theta}_k^-} + \frac{\partial h(\hat{x}_k^-, u_k, \hat{\theta}_k^-)}{\partial \hat{x}_k^-} \frac{d\hat{x}_k^-}{d\hat{\theta}_k^-} \tag{34}
$$

$$
\frac{d\hat{x}_k^-}{d\hat{\theta}_k^-} = \frac{\partial f(\hat{x}_{k-1}^+, u_{k-1}, \hat{\theta}_k^-)}{\partial \hat{\theta}_k^-} + \frac{\partial f(\hat{x}_{k-1}^+, u_{k-1}, \hat{\theta}_k^-)}{\partial \hat{x}_{k-1}^+} \frac{d\hat{x}_{k-1}^+}{d\hat{\theta}_k^-} \tag{35}
$$

$$
\frac{d\hat{x}_{k-1}^+}{d\hat{\theta}_k^-} = \frac{d\hat{x}_{k-1}^-}{d\hat{\theta}_{k-1}^+} - L_{k-1}^x \frac{dh(\hat{x}_{k-1}^-, u_{k-1}, \hat{\theta}_{k-1}^+)}{d\hat{\theta}_{k-1}^+} \tag{36}
$$

For this purpose, $\frac{d\hat{x}_{k-1}^+}{d\hat{\theta}_k^-}$ is initialized to zero and the three total-derivatives are updated recursively.

The parameter vector to be estimated contains the series resistor and the ZARC parameters: $\theta = \begin{bmatrix} R_0 & R_{ZARC} & \tau_{ZARC} & \alpha \end{bmatrix}^T$. According to the state (24) and output Eqs. (25), as well as expressions in Table 2, the Jacobian matrices required in Eqs. (29), (31), (34) and (35) are those calculated in Eqs. (37), (38), (39) and (40), respectively:

$$
F_{k-1}^x = diag\left[1 \quad \exp\left(-\tfrac{\Delta t}{\tau_{1,k}}\right) \quad \exp\left(-\tfrac{\Delta t}{\tau_{2,k}}\right) \quad \dots \quad \exp\left(-\tfrac{\Delta t}{\tau_{7,k}}\right)\right] \tag{37}
$$

$$
H_k^x = \left[\left.\frac{\partial OCV}{\partial SOC}\right|_{SOC = \hat{SOC}_k^-} \quad R_{1,k} \quad R_{2,k} \quad \dots \quad R_{7,k}\right] \tag{38}
$$

$$
\begin{aligned}
\frac{\partial h(\hat{x}_k, u_k, \hat{\theta}_k^-)}{\partial \hat{\theta}_k^-} = \Big[& i_k \quad r_1(\hat{\alpha}_k^-)\hat{i}_{1,k}^- + r_2(\hat{\alpha}_k^-)\hat{i}_{2,k}^- + \cdots + r_7(\hat{\alpha}_k^-)\hat{i}_{7,k}^-\\
& 0 \quad \hat{R}_{ZARC,k}^- \left(r_1'(\hat{\alpha}_k^-)\hat{i}_{1,k}^- + r_2'(\hat{\alpha}_k^-)\hat{i}_{2,k}^- + \cdots + r_7'(\hat{\alpha}_k^-)\hat{i}_{7,k}^-\right)\Big]
\end{aligned}
\tag{39}
$$

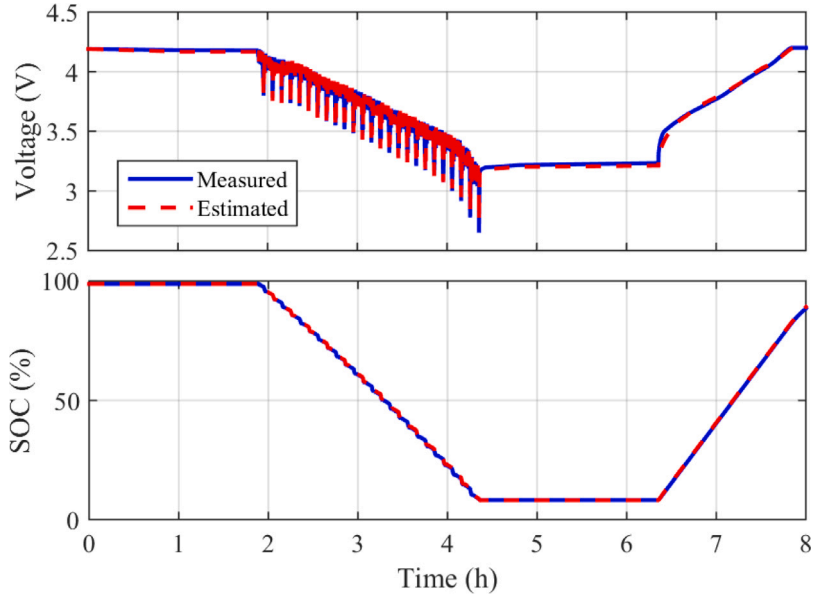

Fig. 13. Experimental and estimated voltage and SOC throughout cycle 1.

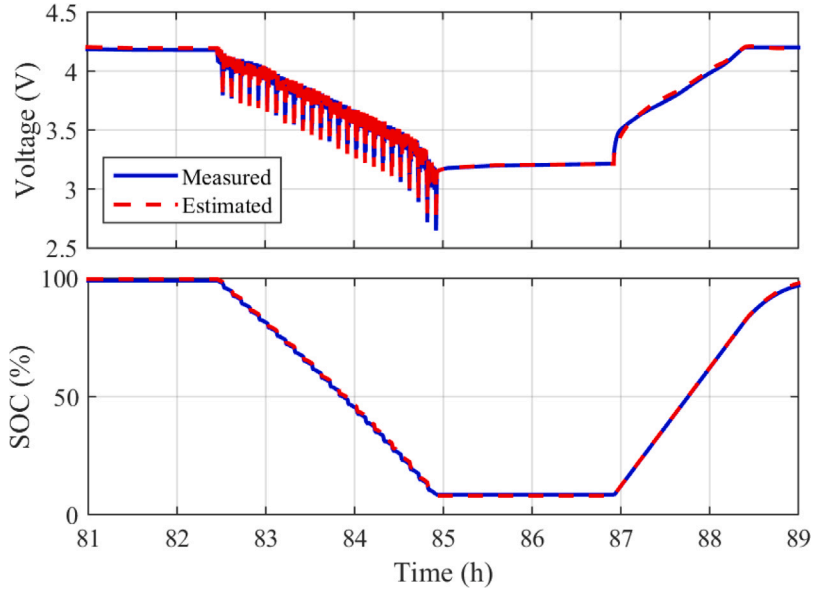

Fig. 14. Experimental and estimated voltage and SOC throughout cycle 10.

$$\frac{\partial f(\hat{x}_{k-1}^{+}, u_{k-1}, \hat{\theta}_{k}^{-})}{\partial \hat{\theta}_{k}^{-}} = \begin{bmatrix} 0 & 0 & 0 & 0 \\ 0 & 0 & A_1 & B_1 \\ 0 & 0 & A_2 & B_2 \\ 0 & 0 & A_3 & B_3 \\ 0 & 0 & A_4 & B_4 \\ 0 & 0 & A_5 & B_5 \\ 0 & 0 & A_6 & B_6 \\ 0 & 0 & A_7 & B_7 \end{bmatrix} \tag{40}$$

where:

$$\begin{aligned} A_1 &= t_1(\hat{\alpha}_k^{-}) \tfrac{\Delta t}{(\tau_{1,k})^2} \exp\left(-\tfrac{\Delta t}{\tau_{1,k}}\right)\left(\hat{i}_{R1,k-1}^{+} - i_{k-1}\right) \\ B_1 &= \hat{\tau}_{ZARC,k}^{-} t_1'(\hat{\alpha}_k^{-}) \tfrac{\Delta t}{(\tau_{1,k})^2} \exp\left(-\tfrac{\Delta t}{\tau_{1,k}}\right)\left(\hat{i}_{R1,k-1}^{+} - i_{k-1}\right) \end{aligned} \tag{41}$$

Once the theoretical framework for the DEKF has been established, the algorithm is initialized by inputting the starting values for both states and parameters. Since the cycling scheme begins with a short rest period, initial SOC is estimated via voltage measurement and the OCV-SOC relationship and initial currents are set to zero in Eq. (42), whereas the state estimation error covariance matrix is initialized in Eq. (43).

$$\hat{x}_0^{+} = \begin{bmatrix} OCV^{-1}(v_0) & 0 & 0 & 0 & 0 & 0 & 0 & 0 \end{bmatrix}^T \tag{42}$$

$$\hat{P}_0^{x} = diag\begin{bmatrix} 10^{-3} & 0 & 0 & 0 & 0 & 0 & 0 & 0 \end{bmatrix} \tag{43}$$

Parameters are initialized to the values calculated in the time-domain identification procedure in Eq. (44), while the parameter estimation error covariance matrix is initially set to a diagonal matrix with the parameter variances shown in Eq. (45):

$$\hat{\theta}_0^{+} = \begin{bmatrix} 0.025 & 0.0627 & 247.25 & 0.5038 \end{bmatrix}^T \tag{44}$$

$$\hat{P}_0^{\theta} = diag\begin{bmatrix} 10^{-6} & 10^{-6} & 1 & 10^{-6} \end{bmatrix} \tag{45}$$

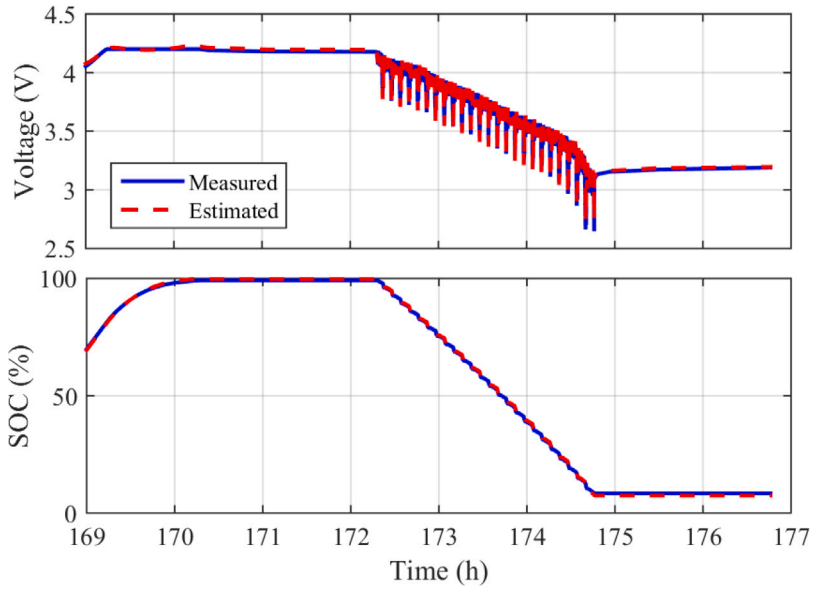

Fig. 15. Experimental and estimated voltage and SOC throughout cycle 20.

In order to ensure the stability and convergence of the state and parameter filters, tuning the covariance matrices corresponding to process and measurement noises of both state and parameter filters Q_0^x, R_0^x Q_0^θ and R_0^θ is required. In this case, covariance matrices have been initialized as in Eq. (46):

$$Q_k^x = 10^{-5} \cdot diag\left[10^{-5} \quad 1 \quad 1 \quad 1 \quad 1 \quad 1 \quad 1 \quad 1\right] \quad R_k^x = 10^{-4}$$
$$Q_k^\theta = diag\left[2 \cdot 10^{-9} \quad 2 \cdot 10^{-9} \quad 2 \cdot 10^{-5} \quad 2 \cdot 10^{-8}\right] \quad R_k^\theta = 10^{-2} \tag{46}$$

5.2. Results

Lastly, the voltage and SOC estimation results obtained by applying the previously described model and DFOEKF are validated with the experimental measurements described in Section 3. As discussed in Sections 1 and 2, the proposed method allows for the estimation of the voltage evolution during prolonged rests and constant-current charge periods, as well as the driving cycle stages. Although parameter values are not expected to change significantly in 20 cycles, estimating them adaptively is justified given the variations they present at different SOCs observed in EIS measurements in Section 4.

Figs. 13–15 show the estimation results throughout the 1st, 10th and 20th complete cycles, respectively. It is observed that this algorithm provides a voltage estimation which is in great agreement with experimental measurements throughout the driving cycle stage as well as the rests and constant-current charging periods once the ZARC parameters have been slightly adjusted. However, there appears to be a minor deviation during the constant-voltage phase, which marginally impacts the SOC estimation in said periods. This issue is likely due to the fact that during the CV stage the input and output of the state-space model are effectively reversed. Nevertheless, estimation errors in these phases are generally considered less critical since the cell operates in tightly controlled conditions, although more accurate simulations of constant-voltage periods with ECMs will be addressed in future research.

Root-mean-square error (RMS) and mean-absolute error (MAE) between estimations and experimental data are 0.28% and 0.18% for SOC, along with 15.2 mV and 9.4 mV for voltage, respectively. It has to be pointed out that the proposed method yields very similar estimation errors to those from recent works that only take into account individual driving cycle data and considerably smaller time frames [30–33]. Only the recent work by Solomon et al. [32] shows the experimental and predicted voltage transients during prolonged rests for a memory length $L_m = 300$, although the voltage evolution during the constant-current charging stage is not shown. A qualitative difference between this approach and the previously cited works is the ability to accurately model the voltage response regardless of the operation stage, with a state-vector size often two orders of magnitude smaller than the required memory length for the same degree of accuracy. Additionally, this method allows for the online updating of the fractional order α, to account for the possible variation of this parameter at different SOCs, ambient temperatures or aging stages.

As discussed in Section 4, the accurate identification of meaningful fractional parameters for time-domain applications is not a trivial procedure that entails solving a complex minimization problem, often by means of metaheuristic algorithms. However, these methods are computationally expensive and inadequate for online applications, requiring offline implementations. For this reason, a precise time-domain parameterization of fractional-order elements is not always readily available. Consequently, the ability to recover from an inaccurate initialization and estimate adequate parameter values is a highly desirable trait in an online monitoring algorithm. In order to test the capabilities of the proposed method, two incorrect parameterizations θ_1 and θ_2, alternative to θ_0 in Eq. (44), are introduced in Eq. (47): the first one with a 20% error in both R_{ZARC} and α, while the second one with a 50% error in all parameter values.

$$\theta_1 = \left[0.025 \quad 0.05 \quad 250 \quad 0.6\right]^T$$
$$\theta_2 = \left[0.038 \quad 0.03 \quad 375 \quad 0.75\right]^T \tag{47}$$

The evolution of the estimated parameters in all three cases is shown in Fig. 16. The error in R_0 is corrected during the first cycle, whereas the R_{ZARC} converges to their corresponding values within several cycles for all three cases. Conversely, α, and particularly τ_{ZARC}, do so in a slower manner. This shows that the voltage sensitivity to the equivalent circuit parameters is not identical, with τ_{ZARC} being the least critical parameter to identify, especially within an operating regime with quick changes in current.

The estimation results for the three different initializations are stated in Table 4. It is noted that the second parameterization only has a reduced effect on the voltage estimation, whereas the third initialization has a greater impact on both estimation errors. This

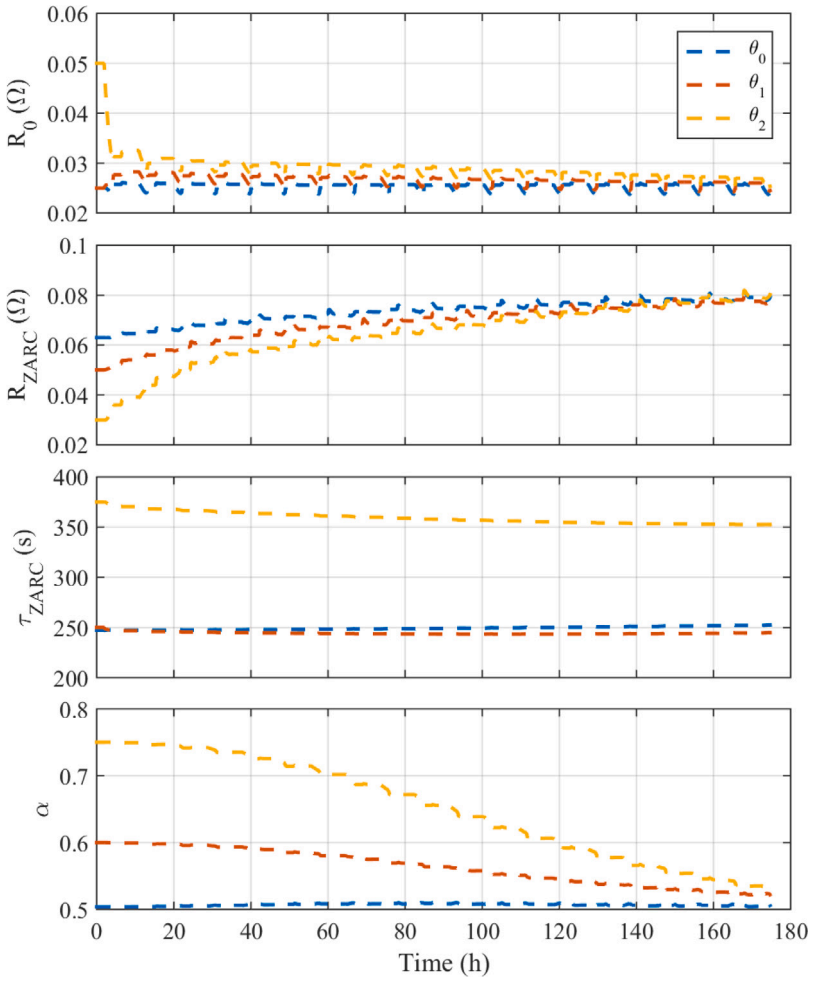

Fig. 16. Evolution of the identified parameters throughout the 20 cycles with correct initialization θ_0 and incorrect initializations θ_1 and θ_2.

Table 4
Summary of estimation results for different parameter initializations.

Error	Voltage (mV)		SOC (%)	
Initialization	RMS	MAE	RMS	MAE
θ_0	15.2	9.4	0.28	0.16
θ_1	15.9	9.5	0.29	0.18
θ_2	21.6	12.8	0.35	0.22

demonstrates the convenience of considering parameter values in an adaptive manner.

As with any Dual Kalman Filter, there exists a trade-off between the state estimation accuracy and the rate of change of the estimated parameters, given by the parameter covariance matrix. If a larger variation in the parameter vector is allowed, the state estimation errors may be decreased at the expense of oscillations in parameter values, which may not be rigorous from a modeling point of view. For this reason, the parameter covariance matrix has been set to a reduced value in order to capture slower variations, which has a direct impact on how quickly our method is able to recover from an incorrect parameter initialization. Another limitation of the proposed method lies on the employed equivalent circuit model. Although fractional-order ECMs are able to provide a more truthful representation of distributed diffusion processes with fewer parameters than standard RC models, they are not as insightful as electrochemical models and fail to account for more complex processes occurring in lithium-ion batteries. Consequently, analyzing the relationship between time-domain and frequency-domain parameter values and establishing the correspondence with the characteristic parameters in electrochemical models remains an open research topic, which warrants the development of more comprehensive fractional-order equivalent circuit models.

6. Conclusions

In this article, we have proposed a novel Dual Fractional-Order Extended Kalman Filter for the simultaneous estimation of state of charge and all fractional parameters based on the multiple-RC approximation of the ZARC element instead of the Grünwald–Letnikov definition of the fractional-order derivative. This allows avoiding the issues that arise from the definition of a memory length when applying the latter approach. The fractional parameters have been identified on a novel NMC811/Si-Gr cell via both EIS tests and time-domain measurements, and the differences between both approaches as well as their suitability for this application are discussed. We have validated the performance of this method experimentally in both driving cycles and slowly-varying operation and its robustness to incorrect initializations, obtaining a SOC RMS error of 0.28% and a voltage RMS error of 15.2 mV in 20 complete charge–discharge cycles. The accurate estimation results of the proposed method along with its validity regardless of the operation stage make it an interesting alternative for its implementation in battery management systems.

CRediT authorship contribution statement

Pablo Rodríguez-Iturriaga: Conceptualization, Methodology, Investigation, Writing – original draft. **Jorge Alonso-del-Valle:** Investigation, Resources, Data curation. **Salvador Rodríguez-Bolívar:** Conceptualization, Methodology, Investigation, Writing – original draft, Writing – review & editing. **David Anseán:** Investigation, Resources, Data curation, Writing – original draft. **Juan Carlos Viera:** Investigation, Resources, Data curation, Supervision. **Juan Antonio López-Villanueva:** Methodology, Investigation, Writing – review & editing, Supervision.

Declaration of competing interest

The authors declare that they have no known competing financial interests or personal relationships that could have appeared to influence the work reported in this paper.

Data availability

Data will be made available on request.

Acknowledgments

This work was partially supported by the Spanish Ministry of Science and Innovation, Spain and by FEDER funds via Project PID2019-110955RB-I00/AEI/10.13039/501100011033 and by the Principality of Asturias, Spain via project AYUD/2021/50994 and by the Regional Government of Andalusia, Spain via project PAIDI 2020 P18-RT-3303, and by Severo Ochoa Program for Predoctoral Scholarships, Spain (PA-18-PF-BP17-134) and by the FPU-UGR-Banco Santander Program for Predoctoral Scholarships.

References

[1] J. Xie, Y.-C. Lu, A retrospective on lithium-ion batteries, Nature Commun. 11 (2020) 2499, http://dx.doi.org/10.1038/s41467-020-16259-9.

[2] G. Zubi, R. Dufo-López, M. Carvalho, G. Pasaoglu, The lithium-ion battery: State of the art and future perspectives, Renew. Sustain. Energy Rev. 89 (2018) 292–308, http://dx.doi.org/10.1016/j.rser.2018.03.002.

[3] D. Stampatori, P.P. Raimondi, M. Noussan, Li-ion batteries: A review of a key technology for transport decarbonization, Energies 13 (10) (2020) http://dx.doi.org/10.3390/en13102638.

[4] G. Berckmans, M. Messagie, J. Smekens, N. Omar, L. Vanhaverbeke, J. Van Mierlo, Cost projection of state of the art lithium-ion batteries for electric vehicles up to 2030, Energies 10 (9) (2017) http://dx.doi.org/10.3390/en10091314.

[5] U.K. Das, P. Shrivastava, K.S. Tey, M.Y.I. Bin Idris, S. Mekhilef, E. Jamei, M. Seyedmahmoudian, A. Stojcevski, Advancement of lithium-ion battery cells voltage equalization techniques: A review, Renew. Sustain. Energy Rev. 134 (2020) 110227, http://dx.doi.org/10.1016/j.rser.2020.110227.

[6] C. Li, N. Cui, Z. Cui, C. Wang, C. Zhang, Novel equivalent circuit model for high-energy lithium-ion batteries considering the effect of nonlinear solid-phase diffusion, J. Power Sources 523 (2021) (2022) 230993, http://dx.doi.org/10.1016/j.jpowsour.2022.230993.

[7] S. Wang, S. Jin, D. Bai, Y. Fan, H. Shi, C. Fernandez, A critical review of improved deep learning methods for the remaining useful life prediction of lithium-ion batteries, Energy Rep. 7 (2021) 5562–5574, http://dx.doi.org/10.1016/j.egyr.2021.08.182.

[8] T.F. Fuller, M. Doyle, J. Newman, Simulation and optimization of the dual lithium ion insertion cell, J. Electrochem. Soc. 141 (1) (1994) 1–10, http://dx.doi.org/10.1149/1.2054684.

[9] T.F. Fuller, J.E. Soc, T.F. Fuller, M. Doyle, J. Newman, Relaxation phenomena in lithium - ion - insertion cells relaxation phenomena in lithium-ion-insertion cells, 1994.

[10] S.G. Marquis, V. Sulzer, R. Timms, C.P. Please, S.J. Chapman, An asymptotic derivation of a single particle model with electrolyte, J. Electrochem. Soc. 166 (15) (2019) A3693–A3706, http://dx.doi.org/10.1149/2.0341915jes.

[11] E. Miguel, G.L. Plett, M.S. Trimboli, L. Oca, U. Iraola, E. Bekaert, Review of computational parameter estimation methods for electrochemical models, J. Energy Storage 44 (2021) 103388, http://dx.doi.org/10.1016/j.est.2021.103388.

[12] S. Wang, P. Takyi-Aninakwa, S. Jin, C. Yu, C. Fernandez, D.-I. Stroe, An improved feedforward-long short-term memory modeling method for the whole-life-cycle state of charge prediction of lithium-ion batteries considering current–voltage-temperature variation, Energy 254 (2022) 124224, http://dx.doi.org/10.1016/j.energy.2022.124224.

[13] Z. Wang, G. Feng, D. Zhen, F. Gu, A. Ball, A review on online state of charge and state of health estimation for lithium-ion batteries in electric vehicles, Energy Rep. 7 (2021) 5141–5161, http://dx.doi.org/10.1016/j.egyr.2021.08.113.

[14] H. Ren, Y. Zhao, S. Chen, L. Yang, A comparative study of lumped equivalent circuit models of a lithium battery for state of charge prediction, Int. J. Energy Res. 43 (2019) 7306–7315, http://dx.doi.org/10.1002/er.4759.

[15] P. Shrivastava, T.K. Soon, M.Y.I.B. Idris, S. Mekhilef, Overview of model-based online state-of-charge estimation using kalman filter family for lithium-ion batteries, Renew. Sustain. Energy Rev. 113 (2019) 109233, http://dx.doi.org/10.1016/j.rser.2019.06.040.

[16] P. Shrivastava, T. Kok Soon, M.Y.I. Bin Idris, S. Mekhilef, S.B.R.S. Adnan, Combined state of charge and state of energy estimation of lithium-ion battery using dual forgetting factor-based adaptive extended kalman filter for electric vehicle applications, IEEE Trans. Veh. Technol. 70 (2) (2021) 1200–1215, http://dx.doi.org/10.1109/TVT.2021.3051655.

[17] J. Gomez, R. Nelson, E.E. Kalu, M.H. Weatherspoon, J.P. Zheng, Equivalent circuit model parameters of a high-power li-ion battery: Thermal and state of charge effects, J. Power Sources 196 (10) (2011) 4826–4831, http://dx.doi.org/10.1016/j.jpowsour.2010.12.107.

[18] D. Chen, L. Xiao, W. Yan, Y. Guo, A novel hybrid equivalent circuit model for lithium-ion battery considering nonlinear capacity effects, Energy Rep. 7 (2021) (2021) 320–329, http://dx.doi.org/10.1016/j.egyr.2021.06.051, 6th International Conference on Advances on Clean Energy Research.

[19] E. Hernández-Balaguera, Numerical approximations on the transient analysis of bioelectric phenomena at long time scales via the mittag-leffler function, Chaos Solitons Fractals 145 (2021) 110768, http://dx.doi.org/10.1016/j.chaos.2021.110768.

[20] C. Ionescu, A. Lopes, D. Copot, J. Machado, J. Bates, The role of fractional calculus in modeling biological phenomena: A review, Commun. Nonlinear Sci. Numer. Simul. 51 (2017) 141–159, http://dx.doi.org/10.1016/j.cnsns.2017.04.001.

[21] P. Bertsias, S. Kapoulea, C. Psychalinos, A.S. Elwakil, Chapter two - a collection of interdisciplinary applications of fractional-order circuits, in: A.G. Radwan, F.A. Khanday, L.A. Said (Eds.), Fractional Order Systems, 1 of Emerging Methodologies and Applications in Modelling, Academic Press, 2022, pp. 35–69, http://dx.doi.org/10.1016/B978-0-12-824293-3.00007-7.

[22] T. Heil, A. Jossen, Continuous approximation of the ZARC element with passive components, Meas. Sci. Technol. 32 (10) (2021) 104011, http://dx.doi.org/10.1088/1361-6501/ac0466.

[23] D. Andre, M. Meiler, K. Steiner, C. Wimmer, T. Soczka-Guth, D. Sauer, Characterization of high-power lithium-ion batteries by electrochemical impedance spectroscopy. i. experimental investigation, J. Power Sources 196 (12) (2011) 5334–5341, http://dx.doi.org/10.1016/j.jpowsour.2010.12.102, selected papers presented at the 12th Ulm ElectroChemical Talks (UECT):2015 Technologies on Batteries and Fuel Cells.

[24] T. Momma, M. Matsunaga, D. Mukoyama, T. Osaka, Ac impedance analysis of lithium ion battery under temperature control, J. Power Sources 216 (2012) 304–307, http://dx.doi.org/10.1016/j.jpowsour.2012.05.095.

[25] N. Meddings, M. Heinrich, F. Overney, J.S. Lee, V. Ruiz, E. Napolitano, S. Seitz, G. Hinds, R. Raccichini, M. Gaberšček, J. Park, Application of electrochemical impedance spectroscopy to commercial li-ion cells: A review, J. Power Sources 480 (May) (2020) http://dx.doi.org/10.1016/j.jpowsour.2020.228742.

[26] S. Alavi, C. Birkl, D. Howey, Time-domain fitting of battery electrochemical impedance models, J. Power Sources 288 (2015) 345–352, http://dx.doi.org/10.1016/j.jpowsour.2015.04.099.

[27] D. Andre, M. Meiler, K. Steiner, H. Walz, T. Soczka-Guth, D. Sauer, Characterization of high-power lithium-ion batteries by electrochemical impedance spectroscopy. ii: Modelling, J. Power Sources 196 (12) (2011) 5349–5356, http://dx.doi.org/10.1016/j.jpowsour.2010.07.071, selected papers presented at the 12th Ulm ElectroChemical Talks (UECT):2015 Technologies on Batteries and Fuel Cells.

[28] T.P. Heins, N. Schlüter, S.T. Ernst, U. Schröder, On the interpretation of impedance spectra of large-format lithium-ion batteries and its application in aging studies, Energy Technol. 8 (2) (2020) 1900279, http://dx.doi.org/10.1002/ente.201900279.

[29] I. Podlubny, Fractional differential equations, 1999.

[30] L. Su, G. Zhou, D. Hu, Y. Liu, Y. Zhu, Research on the state of charge of lithium-ion battery based on the fractional order model, Energies 14 (2021) http://dx.doi.org/10.3390/en14196307.

[31] L. He, Y. Wang, Y. Wei, M. Wang, X. Hu, Q. Shi, An adaptive central difference kalman filter approach for state of charge estimation by fractional order model of lithium-ion battery, Energy 244 (2022) 122627, http://dx.doi.org/10.1016/j.energy.2021.122627.

[32] O.O. Solomon, W. Zheng, J. Chen, Z. Qiao, State of charge estimation of lithium-ion battery using an improved fractional-order extended kalman filter, J. Energy Storage 49 (2022) 104007, http://dx.doi.org/10.1016/j.est.2022.104007.

[33] K.S. Mawonou, A. Eddahech, D. Dumur, D. Beauvois, E. Godoy, Improved state of charge estimation for li-ion batteries using fractional order extended kalman filter, J. Power Sources 435 (2019) 226710, http://dx.doi.org/10.1016/j.jpowsour.2019.226710.

[34] X. Hu, H. Yuan, C. Zou, Z. Li, L. Zhang, Co-estimation of state of charge and state of health for lithium-ion batteries based on fractional-order calculus, IEEE Trans. Veh. Technol. 67 (2018) 10319–10329, http://dx.doi.org/10.1109/TVT.2018.2865664.

[35] T. Ouyang, P. Xu, J. Lu, X. Hu, B. Liu, N. Chen, Coestimation of state-of-charge and state-of-health for power batteries based on multithread dynamic optimization method, IEEE Trans. Ind. Electron. 69 (2) (2022) 1157–1166, http://dx.doi.org/10.1109/TIE.2021.3062266.

[36] Z. Yu, R. Huai, H. Li, Cpso-based parameter-identification method for the fractional-order modeling of lithium-ion batteries, IEEE Trans. Power Electron. 36 (10) (2021) 11109–11123, http://dx.doi.org/10.1109/TPEL.2021.3073810.

[37] A. Oustaloup, F. Levron, B. Mathieu, F. Nanot, Frequency-band complex noninteger differentiator: characterization and synthesis, IEEE Trans. Circuits Syst. I 47 (1) (2000) 25–39, http://dx.doi.org/10.1109/81.817385.

[38] G. Tsirimokou, A systematic procedure for deriving rc networks of fractional-order elements emulators using matlab, AEU - Int. J. Electron. Commun. 78 (2017) 7–14, http://dx.doi.org/10.1016/j.aeue.2017.05.003.

[39] A. Farmann, W. Waag, D.U. Sauer, Adaptive approach for on-board impedance parameters and voltage estimation of lithium-ion batteries in electric vehicles, J. Power Sources 299 (2015) 176–188, http://dx.doi.org/10.1016/j.jpowsour.2015.08.087.

[40] S.-H. Kim, W. Choi, K.-B. Lee, S. Choi, Advanced dynamic simulation of supercapacitors considering parameter variation and self-discharge, IEEE Trans. Power Electron. 26 (11) (2011) 3377–3385, http://dx.doi.org/10.1109/TPEL.2011.2136388.

[41] J.A. López-Villanueva, P. Rodríguez-Iturriaga, L. Parrilla, S. Rodríguez-Bolívar, A compact model of the zarc for circuit simulators in the frequency and time domains, AEU - Int. J. Electron. Commun. (2022) 154293, http://dx.doi.org/10.1016/j.aeue.2022.154293.

[42] B.O. Agudelo, W. Zamboni, E. Monmasson, A comparison of time-domain implementation methods for fractional-order battery impedance models, Energies 14 (2021) 1–23, http://dx.doi.org/10.3390/en14154415.

[43] P. Shen, M. Ouyang, L. Lu, J. Li, X. Feng, The co-estimation of state of charge, state of health, and state of function for lithium-ion batteries in electric vehicles, IEEE Trans. Veh. Technol. 67 (1) (2018) 92–103, http://dx.doi.org/10.1109/TVT.2017.2751613.

[44] L. Vichard, A. Ravey, P. Venet, F. Harel, S. Pelissier, D. Hissel, A method to estimate battery soh indicators based on vehicle operating data only, Energy 225 (2021) 120235, http://dx.doi.org/10.1016/j.energy.2021.120235.

[45] USABC, Electric Vehicle Battery Test Procedures Manual. Revision,Vol. 2, Tech. rep., 1996, http://dx.doi.org/10.2172/214312.

[46] M. Dubarry, G. Baure, Perspective on commercial li-ion battery testing, best practices for simple and effective protocols, Electronics 9 (1) (2020) http://dx.doi.org/10.3390/electronics9010152.

[47] X.-S. Yang, Chapter 7 - particle swarm optimization, in: X.-S. Yang (Ed.), Nature-Inspired Optimization Algorithms, Elsevier, Oxford, 2014, pp. 99–110, http://dx.doi.org/10.1016/B978-0-12-416743-8.00007-5.

[48] J. Wu, C. Fang, Z. Jin, L. Zhang, J. Xing, A multi-scale fractional-order dual unscented kalman filter based parameter and state of charge joint estimation method of lithium-ion battery, J. Energy Storage 50 (2022) 104666, http://dx.doi.org/10.1016/j.est.2022.104666.

[49] K.D. Rao, A.H. Chander, S. Ghosh, Robust observer design for mitigating the impact of unknown disturbances on state of charge estimation of lithium iron phosphate batteries using fractional calculus, IEEE Trans. Veh. Technol. 70 (4) (2021) 3218–3231, http://dx.doi.org/10.1109/TVT.2021.3066249.

[50] A. Farmann, W. Waag, D.U. Sauer, Application-specific electrical characterization of high power batteries with lithium titanate anodes for electric vehicles, Energy 112 (2016) 294–306, http://dx.doi.org/10.1016/j.energy.2016.06.088.

[51] D.U.S. Alexander Farmann, Comparative study of reduced order equivalent circuit models for on-board state-of-available-power prediction of lithium-ion batteries in electric vehicles, Appl. Energy 225 (2018) 1102–1122, http://dx.doi.org/10.1016/j.apenergy.2018.05.066.

[52] S. Nejad, D. Gladwin, D. Stone, A systematic review of lumped-parameter equivalent circuit models for real-time estimation of lithium-ion battery states, J. Power Sources 316 (2016) 183–196, http://dx.doi.org/10.1016/j.jpowsour.2016.03.042.